Control of photoelectron interference dynamics with two-color laser fields

Facheng Jin,[1,3] Weifeng Yang,[2,*] Xiwang Liu,[2] Hongdan Zhang,[2] Wenhui Dong,[1] Xiaohong Song,[2,†] and Jing Chen[4,5,‡]
[1]*Research Center for Advanced Optics and Photoelectronics, Department of Physics, College of Science, Shantou University, Shantou, Guangdong 515063, China*
[2]*Department of Physics, School of Science, Hainan University, Haikou 570288, China*
[3]*Faculty of Science, Xi'an Aeronautical Institute, Xi'an 710077, China*
[4]*Institute of Applied Physics and Computational Mathematics, P.O. Box 8009, Beijing 100088, China*
[5]*HEDPS, Center for Applied Physics and Technology, Peking University, Beijing 100084, China*

(Received 21 September 2021; accepted 24 January 2022; published 22 February 2022)

We study the multiple interference structures in photoelectron momentum distributions (PMDs) of xenon atoms, whose dynamics can be manipulated effectively by a fundamental and weaker third-harmonic two-color laser fields, especially for an oblique interference pattern. It is found that this structure is only attributed to the contributions from the forward-scattered electrons as a Coulomb effect in strong-field physics. Further, the gross structure of the oblique interference arises from the forward-scattered electron ionized within a quarter-cycle of the fundamental field, and the fine structure is identified to originate from the intercycle interference of the trajectories. Moreover, we demonstrate that the multiple interference structure can be enhanced or suppressed by adjusting the relative phase of two colors. Our investigation shows that the two-color laser fields can be tailored with the purpose of manipulating specific dynamics process, which will be helpful to resolve ultrafast spatio-temporal information from the complex interference in strong-field ionization.

DOI: 10.1103/PhysRevResearch.4.013140

I. INTRODUCTION

When an atom or a molecule is illuminated with an intense laser field, the electron wave packet (EWP) may follow different quantum paths from its bound state to the continuum state in the combined laser and Coulomb fields [1–8]. The coherent superposition of these EWPs can create rich interference structures in the final photoelectron momentum distributions (PMDs) [9–12]. Particularly, a high-resolution holographic interference was observed experimentally in the PMDs of metastable xenon atom irradiated with a midinfrared free-electron laser source [13,14]. The holographic structure can be defined as those generated by the interference of direct EWPs (the reference), which is no interaction with the core subsequent to ionization, with those scattered EWPs with the core (a signal) [15]. This definition has been extended and generalized, which refers to holographic patterns also as a result of the interference undergoing different types of rescattering pathways [16]. The photoelectron interference records the magnitude and the phase of photoelectron scattering amplitudes [17,18], which has been a powerful imaging technique with the ultrafast time resolution [19–28]. Well known holographic examples are the spiderlike [13,29,30], carpetlike [31], fanlike [32,33], and fork- [28] or fishbone-like [27,34,35] structures. The spiderlike structure is caused by the interference of the direct EWPs and the laser-driven forward-scattered EWPs from the same quarter-cycle of the laser pulse [13,29]. The residual Coulomb potential may result in an angle-dependent, radial distortion in a pattern, which can be called as the temporal double-slit interference [36,37]. The fanlike pattern that forms near the threshold may stem from the interference between direct and forward deflected EWPs [37]. The fishbonelike structure may be viewed as a holographic pattern resulting from backscattered EWPs interfering with direct EWPs, and is particularly sensitive to the target structure [15,34].

It is a known fact that numerous interesting interference structures in the PMDs inherently encode the temporal and spatial information of the ions and electrons [11]. However, it is a major challenge to explore the multiple dynamics of electrons from the complex interference patterns and to achieve coherent control of EWPs in strong-field community. Currently, a two-color laser field by their tunable parameters can manipulate effectively specific types of EWPs [38–41], which may be in favor of uncovering and analyzing the dynamic process for different interference patterns. In Ref. [42], a phase-controlled orthogonal two-color laser pulse is employed to study the photoemission dynamic of Freeman resonance via the $4f$ and $5p$ Rydberg states of argon atom. Different photoemission pathways in the ionization process were disentangled by controlling the relative phase of two lasers, the origin of the time delays had been

---

[*] wfyang@hainanu.edu.cn
[†] song_xiaohong@hainanu.edu.cn
[‡] chen_jing@iapcm.ac.cn

traced to retrapped resonant ionization [43]. More recently, a deep-learning-performed strong-field Feynman's formulation (DLPSFFF) was proposed to extract effectively the information of electron dynamics and predict the new interference structure [44]. It is worth noting that an oblique interference structure was clearly predicted by using DLPSFFF in single-color laser field [44]. In this paper, we show that the multiple interference patterns, including the oblique structure, can be controlled by employing a two-color field consisting of a fundamental and its weaker third-harmonic fields. The formation of these structures and field-induced dynamics are explored. Especially, the underlying physical mechanism for a new fine oblique structure is revealed.

Our article is organized as the following. We briefly introduce the numerical methods for solving the time-dependent Schrödinger equation (TDSE) and the Coulomb-corrected strong-field approximation (CCSFA) methods in Sec. II; the classical model to investigate the dynamics of the oblique interference structure is presented in Sec. III. The conclusion is given in Sec. IV. In our discussion, atomic units (a.u.) are used throughout unless specified otherwise.

II. METHOD

In this section, we will briefly summarize the numerical solution of the TDSE method, and the CCSFA approach based on the application of the Feynman's path-integral formalism. The numerical result of the TDSE can be used as a benchmark for assessing the validity of the CCSFA simulations.

A. The numerical solution of the time-dependent Schrödinger equation

To investigate the PMDs of atoms induced by a two-color field, we resort to the three-dimensional TDSE [45] with the single-active-electron (SAE) approximation, spherically symmetric Coulomb potential, and in dipole approximation. The TDSE in the velocity gauge reads

$$\begin{aligned} i\frac{\partial}{\partial t}\Psi(\mathbf{r},t) &= \bar{H}\Psi(\mathbf{r},t), \\ \bar{H} &= -\frac{1}{2}\nabla^2 - i\mathbf{A}(t)\cdot\nabla + V(r). \end{aligned} \tag{1}$$

Here $\bar{H}$ is the Hamiltonian operator, the vector potential of the external laser field is given by $\mathbf{A}(t) = -\int_0^t \mathbf{E}(t')dt'$ with the corresponding electric field $\mathbf{E}(t)$, and $\nabla = i\hat{\mathbf{p}}$ with $\hat{\mathbf{p}}$ denoting the momentum operator. The Coulomb potential of the atom is expressed by [45]

$$V(r) = \begin{cases} -1.0/\sqrt{r^2+\alpha^2} & r < R_{co}, \\ -(2R_{co}-r)/R_{co}^2 & R_{co} \leqslant r < 2R_{co}, \\ 0 & r \geqslant 2R_{co}, \end{cases} \tag{2}$$

where R_{co} is the cutoff radius, and α is the soft-core parameter. The total wave function is expanded in spherical harmonics,

$$\Psi(\mathbf{r},t) = \frac{1}{r}\sum_{l=0}^{\infty}\sum_{m=-l}^{l}\phi_{lm}(r,t)Y_{lm}(\Omega). \tag{3}$$

In the above, $\phi_{lm}(r,t)$ is the radial function, $Y_{lm}(\Omega)$ is a spherical harmonic function. l (m) is the angular (magnetic) momentum quantum number. In this calculation, we now consider a two-color linearly polarized laser field. The polarization direction is along z axis and the electric field can be expressed in the form

$$\mathbf{E}(t) = f(t)[E_0\cos(\omega t) + E_1\cos(3\omega t + \varphi)]\mathbf{e}_z. \tag{4}$$

In our TDSE calculation, the pulse envelope can be expressed as $f(t) = \sin^2(\pi t/\tau_p)$ with $\tau_p = 6T_{1600\,\mathrm{nm}}$, and $\mathrm{T}_{1600\,\mathrm{nm}}$ denotes the unit of period of fundamental field. In Eq. (4), E_0 and E_1 are the strengths of the fundamental and the third-harmonic fields, respectively. ω is the laser frequency of the fundamental field, and φ is the relative phase of the two colors. In Eq. (2), α and R_{co} are separately set to be 0.04 a.u. and 100.0 a.u. such that they match the ionization potential of xenon atom $I_p = 0.446$ a.u. and satisfy convergence accuracy.

B. The Coulomb-corrected strong-field approximation method

The semiclassical model provides an intuitive background for exact theories and has direct implications for the interference structures. To reveal the underlying mechanism of these interference structures, we apply the CCSFA to calculate the PMDs.

The EWP of a free electron in an external electronic field is quantum mechanically described by Gordon-Volkov states. In the non-relativistic limit, the Gordon-Volkov wave function in velocity gauge can be written as [16,46,47],

$$\psi_{\mathbf{p}}^{(\mathrm{GV,V})}(\mathbf{r},t) = \frac{1}{(2\pi)^{3/2}}\exp\left\{i\left[(\mathbf{p}+\mathbf{A}(t))\cdot\mathbf{r} - \frac{1}{2}\int_0^t dt'(\mathbf{p}+\mathbf{A}(t'))^2\right]\right\}. \tag{5}$$

In the strong-field approximation (SFA), the final state can be substituted by Gordon-Volkov state, $\langle\psi_{\mathbf{p}}(t_f)| \to \langle\psi_{\mathbf{p}}^{(\mathrm{GV})}(t_f)|$, then the transition amplitude of electron from initial ground state ψ_0 with binding potential $-I_p$ to the continuum state $\psi_{\mathbf{p}}^{(\mathrm{GV})}$ of asymptotic momentum $\mathbf{p}$ in the length gauge can be described by

$$M_{\mathbf{p}}(t_f,t_i) = -i\int_{t_i}^{t_f} d\tau\big\langle\psi_{\mathbf{p}}^{(\mathrm{GV})}(\tau)|\hat{W}(\tau)|\psi_0(\tau)\big\rangle, \tag{6}$$

where $\hat{W}(t) = \mathbf{r}\cdot\mathbf{E}(t)$ is the interaction with the external field. Due to the large amount of calculation for solving the saddle-point equation under the sin-squared envelope with duration $6T_{1600\,\mathrm{nm}}$ conditions, the half-trapezoidal envelope in the semiclassical model

$$f(t) = \begin{cases} 1.0 & 0 \leqslant t < 2T_{1600\,\mathrm{nm}}, \\ \frac{3T_{1600\,\mathrm{nm}}-t}{T_{1600\,\mathrm{nm}}} & 2T_{1600\,\mathrm{nm}} \leqslant t < 3T_{1600\,\mathrm{nm}} \\ 0 & t \geqslant 3T_{1600\,\mathrm{nm}} \end{cases} \tag{7}$$

is used, which can work well with the our TDSE results. It has verified that the two different envelopes will not significantly affect the oblique interference pattern in our calculation. Substituting the Gordon-Volkov state into Eq. (6), the transition matrix element is rewritten as

$$M_{\mathbf{p}}(t_f, t_i) = -i\int_{t_i}^{t_f} d\tau \langle \mathbf{p}+\mathbf{A}(\tau)|\mathbf{r}\cdot\mathbf{E}(\tau)|\psi_0\rangle e^{iS_{I_p,\mathbf{p}}(\tau)}. \quad (8)$$

Since the action $S_{I_p,\mathbf{p}}$ in Eq. (8) is a rapidly oscillating function, the saddle-point approximation is resorted to simplify the transition matrix. The saddle point $t_s^{(\alpha)}$ satisfies the saddle point equation

$$\frac{\partial S_{I_p,\mathbf{p}}}{\partial t}|_{t_s^{(\alpha)}} = 0 \quad \Rightarrow \quad \frac{1}{2}\left(\mathbf{p}+\mathbf{A}\left(t_s^{(\alpha)}\right)\right)^2 = -I_p. \quad (9)$$

Here $I_p > 0$ and $\mathbf{p}$ is real, it is easy to figure out that $t_s^{(\alpha)}$ is a complex, i.e., $t_s^{(\alpha)} = t_r^{(\alpha)} + it_i^{(\alpha)}$, where α denotes a quantum trajectory. Further the corresponding action integral $S_{I_p,\mathbf{p}}(t_s^{(\alpha)})$ can be separated into two parts [48]

$$\begin{aligned} S_{I_p,\mathbf{p}}\left(t_r^{(\alpha)}\right) = &-\int_{t_s^{(\alpha)}}^{t_r^{(\alpha)}}\left(\frac{1}{2}\mathbf{v}^2(\tau)+I_p\right)d\tau \\ &-\int_{t_r^{(\alpha)}}^{T_p}\left(\frac{1}{2}\mathbf{v}^2(\tau)-\frac{Z}{|\mathbf{r}(\tau)|}+I_p\right)d\tau, \end{aligned} \quad (10)$$

where the effective charge is set to be $Z = 2\sqrt{I_p}$, $\mathbf{v}(\tau)$ is the instantaneous velocity of the electron, and T_p is the time of laser switched off. It is worth mentioning that the first and second terms on the right of Eq. (10) are the sub-barrier and the real-time contributions to the phase, respectively [13,49]. Thus using the contour integral of passing near a saddle-point in the complex plane, the integration over τ in Eq. (8) is recast in the form of a sum over all saddle points $t_s^{(\alpha)}$ [50],

$$M_{\mathbf{p}} \sim \sum_{\alpha}\frac{(2I_p)^{5/4}}{\sqrt{2}E\left(t_s^{(\alpha)}\right)\left[\mathbf{p}+\mathbf{A}\left(t_s^{(\alpha)}\right)\right]}e^{iS_{I_p,\mathbf{p}}(t_s^{(\alpha)})}, \quad (11)$$

which indicates the transition amplitude from the bound state to the continuum state of asymptotic momentum $\mathbf{p}$ is a coherent superposition of contributions from all quantum trajectories. Equations (11) and (9) offer deeper physical insight into the ionization process by using "quantum trajectories" to describe the movement of electron in sub-barrier. The complex trajectories are a natural extension of classical trajectories, which are calculated by Newton's equation of motion. For a certain trajectory, the initial velocity while tunneling out at time t_r can be written as $\mathbf{v}_0(t_r) = \mathbf{A}(t_r) + \mathbf{p}$, and the initial position can be defined as the real displacement $\mathbf{r}_0(t_r) = \mathrm{Re}(\int_{t_s}^{t_r}\mathbf{A}(t')dt')$ [51]. After tunneling, the motion of the electron in the real-time propagation is determined by classical trajectory, which can be described by Newton's equations: $\dot{\mathbf{r}}(t) = \mathbf{p}(t)$ and $\dot{\mathbf{p}}(t) = -Z\mathbf{r}(t)/|\mathbf{r}(t)|^3 - \mathbf{E}(t)$. After the electric field is switched off, the motion of the electron is governed by the Coulomb force and follows Kepler's law [52].

III. RESULTS AND DISCUSSION

A. The multiple interference dynamics

In our simulations, the wavelength of the fundamental field is $\lambda = 1600$ nm, the peak intensities of the fundamental and the third-harmonic fields are 150×10^{12} W/cm^2 and 9.4×10^{12} W/cm^2, respectively. In our calculation, the interference structures in PMD can be efficiently controlled by changing the relative phase in this two-color laser field. Figure 1(a) presents a two-color linearly polarized laser field of the first two cycle with relative phase $\varphi = 0$ to clearly show the ionization window. In CCSFA simulation, we just considered electrons emitted in the platform region of the electric fields. Figures 1(b) and 1(c) show the multiple interference structures in PMDs calculated by solving TDSE and CCSFA methods, respectively. The CCSFA simulation reproduces well the main interference features of the TDSE result. There are five types of interference structures clearly observed from both the TDSE and the CCSFA simulations: (I) In Fig. 1(b), the first one is the ringlike structure (black thin solid lines) in low momentum part, formed with the above-threshold ionization peaks [53]. This interference stems from the direct electrons tunneling ionized during two adjacent cycles [50] at the time windows A2-A3 and B2-B3. (II) The second type is the fishbonelike interference pattern (black-thick-solid lines) [15,34], which arises from the interference between directly ionized electrons and backscattered electrons in half-cycles of the time windows A1-A4. (III) The third one, the superposition of the two structures forms a new ringlike interference structure (black-thin-dash lines), which is different from the ATI structure with the center at the origin [6]. (IV) The fourth type

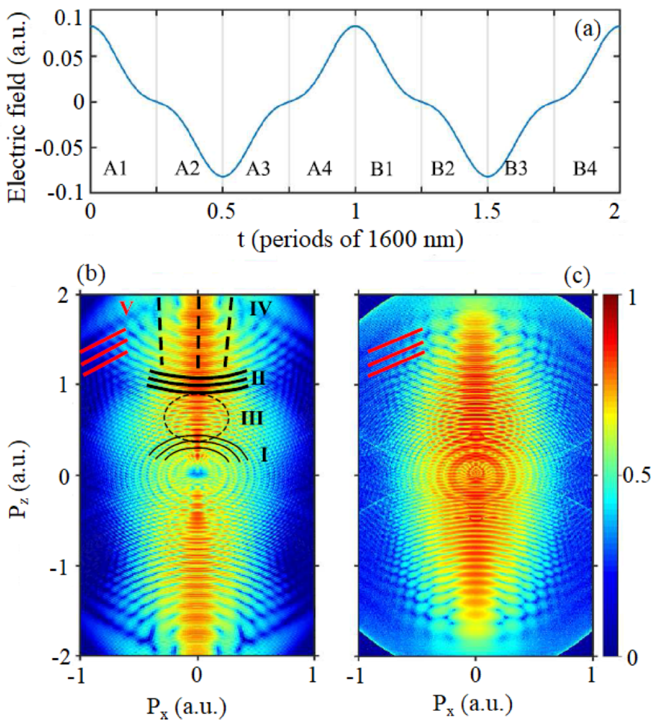

FIG. 1. (a) Electric field of the first two cycles with the fundamental 1600 nm and the third-harmonic fields, where peak intensities are 150×10^{12} W/cm^2 and 9.4×10^{12} W/cm^2, respectively, and relative phase $\varphi = 0$ by using half-trapezoidal envelope. [(b), (c)] PMDs calculated by the TDSE and CCSFA, respectively, where the sin^2 and half-trapezoidal envelope functions are separately used in the TDSE and CCSFA methods (on a logarithmic scale).

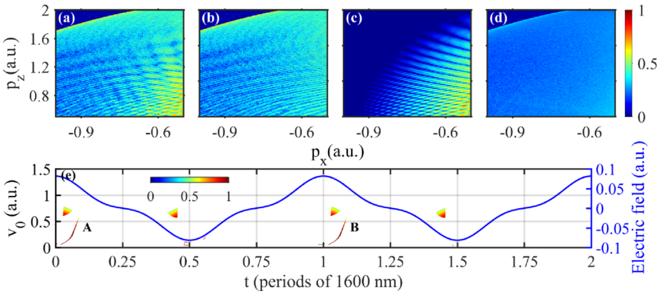

FIG. 2. PMDs simulated by CCSFA and initial conditions of this region. (a) All the electrons are considered, (b) only rescatter electrons are considered, (c) only direct electrons are considered, (d) only rescatter electrons are considered without coherent phase. (e) The initial conditions for the final velocity range are selected. The symbols A and B represent the scattered electrons, where the parameters are the same as that in Fig. 1 (on a logarithmic scale).

is the spiderlike holographic interference fringes (black-thick-dash lines), which are almost straight at large longitudinal momentum originating from the interference of the electrons reaching the detector directly after tunneling and those with a near-forward rescattering with the parent ion at time windows A2-A3 [13]. (V) Here we show a interference pattern called as the oblique structure in this paper, marked by the red-solid lines in Figs. 1(b) and 1(c), where this structure had been clearly predicted by using DLPSFFF approach [44]. It is noted that the oblique structure in the CCSFA is much fainter than that in the TDSE, which is because that the number of the total trajectories (i.e., 1.6×10^8) in our CCSFA simulation is not big enough. In our previous paper [44], the result of the DLPSFFF had been shown that if the total trajectories number is large enough in the CCSFA, the oblique structure will be close to the result of TDSE. To gain more insight into the origin of the interference structure, we analyze all electron trajectories contributing to the momentum spectrum with final momenta in the range 0.8 a.u.$< p_z <$ 2.0 a.u. and -1.0 a.u.$< p_x < -0.5$ a.u., as shown in Fig. 2(a). In this region, the initial conditions of the direct electron and the scattered electron are clearly separated, as shown in Fig. 2(e). It is shown that the contribution of the direct electrons is distributed in the regions around $v_0 = 0.75$ a.u., and appears near each peak of electric field. While the contribution of the scattered electrons (labeled by A and B) is distribution in the regions $v_0 < 0.50$ a.u. and mainly appears after peak of electric field. By comparisons with the interference structures from contributions of the scattered and direct electrons as shown in Figs. 2(b) and 2(c), one can see that the oblique structure arises from the contributions of the scattered electrons. Figure 2(d) shows the contributions of the scattered electrons without interference effect. It indicates that the oblique structure is only attributed to the coherent contributions from the scattered EWPs with different phases. Here we will discuss the contributions of scattered electrons A and B to the oblique interference structure. Figure 3(a) represents the contribution from only the scattered electrons A. It can be seen that the scattered electrons A from a quarter-cycle of the fundamental field can form the gross interference structure. While the intercycle interferences from both the scattered electrons A and B can result in the fine structure, as shown in Fig. 3(b). It is well known that the tunneling electrons may be scattered many times by the joint influence of the laser field and Coulomb potential. Figures 3(c) and 3(d) present contributions from the scattered electrons A in the single and double scattering processes, respectively. It is shown that the single scattering process makes a dominant contribution to the formation of the oblique interference structure, and the contributions of double or even higher scattering can be ignored according to our calculation. Hence we only consider the single scattered process to contribution of the oblique interference structure in the following. In order to further uncover the dynamic information of the oblique interference structure, we will give an intuitive physical interpretation by analyzing the trajectories and corresponding phases of the ionized electrons in the ionization process. Without loss of generality, the trajectories with the final momenta $(p_x, p_z) = (-0.8531, 1.348)$ a.u. as a constructive interference point, and $(-0.8981, 1.232)$ a.u. as a destructive interference point, marked separately by the closed circle and triangle symbols in Fig. 3(a), are used to discuss the interference between different scattered electrons.

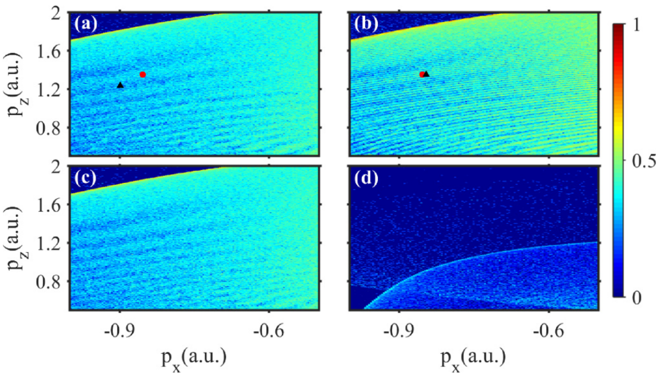

FIG. 3. PMDs of different contributions from the scattered electrons labeled as A (a), both A and B (b), as well as the single (c) and double (d) scattering processes from scattered electrons A, respectively. In (a), the circle and triangle symbols correspond to the final momenta $(p_x, p_z) = (-0.8531, 1.348)$ and $(-0.8981, 1.232)$ a.u., where the first and second points are from the constructive and destructive stripes, respectively. In (b), the circle and triangle symbols correspond to the final momenta $(p_x, p_z) = (-0.8531, 1.348)$ and $(-0.8456, 1.348)$ a.u., which are from the adjacent constructive and destructive fine stripes, respectively (on a logarithmic scale).

Figure 4(a) presents the distributions of phases and the corresponding ionization probabilities for different trajectories with the same final momentum $(-0.8531, 1.348)$ a.u. It is shown that there are some trajectories making contributions to the final momentum [54]. In Fig. 4(a), (t_i, p_{x0}, p_{z0}) represents the initial momentum (p_{x0}, p_{z0}) of the electron ionized at time t_i. One can find that the ionization probability is larger and the initial transverse momentum p_{x0} is smaller as the electron is ionized nearer to the crest of the laser field. As a result, these trajectories can be mainly classified into two categories according to the ionization time t_i, i.e., trajectories with the lower ionization probability for $t_i = 15.4$ a.u., trajectories with the larger ionization probability for $t_i = 9.96$ a.u. Further the two categories can be represented by two equivalent

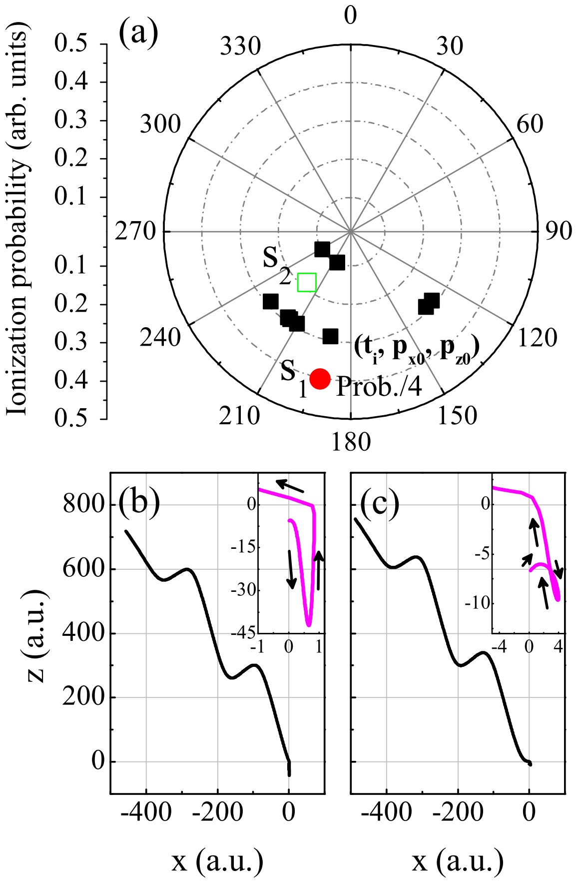

FIG. 4. (a) The closed squares show distributions of phases and the corresponding ionization probabilities for different trajectories with the same final momentum $(p_x, p_z) = (-0.8531, 1.348)$ a.u. as shown by the closed circle in Fig. 3, and the ionization probabilities near the values 0.3 and 0.1 are corresponding to the initial conditions (9.96, 0.0169, 0.122) and (15.4, 0.203, 0.251) a.u., respectively. The closed circle labeled by s_1 and hollow square labeled by s_2 represent the equivalent phases and corresponding probabilities for trajectories born at $t_i = 9.96$ and 15.4 a.u., where the ionization probability of s_1 is divided by 4. [(b),(c)] Typical trajectories for ionization time $t_i =$ 9.96 and 15.4 a.u., respectively, where the insets are the enlargements near the origin and the black arrows indicate the movement direction of the ionized electron.

trajectories: the equivalent ionization probability is a coherent sum by $P = |\sum_j P_j e^{i\varphi_j}|$, and the equivalent phase is given by $\psi = \arg(\sum_j P_j e^{i\varphi_j})$, where P_j and φ_j are the probability and phase of a certain trajectory j. For $t_i = 9.96$ a.u., there are seven trajectories, so the equivalent ionization probability and phase separately are $P_{s_1} = 1.61$ and $\psi_{s_1} = 191.8^\circ$, as marked by the closed circle (s_1) in Fig. 4(a). For $t_i = 15.4$ a.u., there are two trajectories, so $P_{s_2} = 0.186$ and $\psi_{s_2} = 221.0^\circ$, as shown by the hollow square (s_2). The phase difference between two equivalent trajectories is about $\pi/6$ (i.e., smaller than $\pi/2$), while P_{s_1} is much larger than P_{s_2}. Hence the equivalent trajectory s_1 makes a dominant contribution to the ionization process, which can result in the formation of gross interference structure from the the scattered electron ionized within a quarter-cycle of the fundamental field.

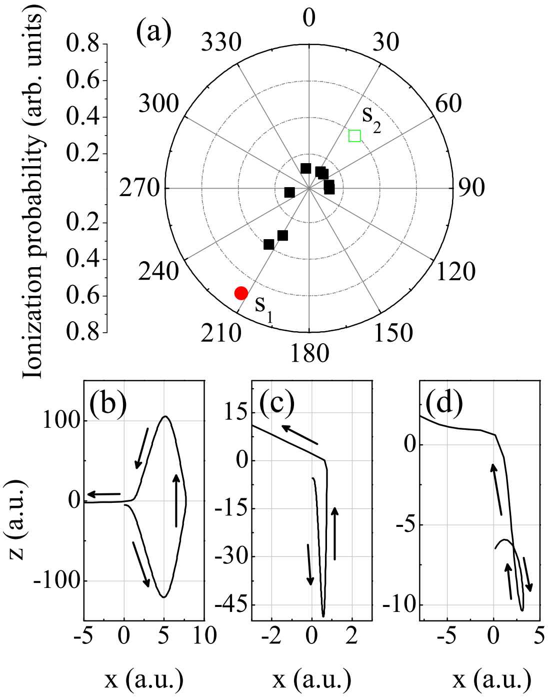

FIG. 5. (a) The closed squares show distributions of phases and the corresponding ionization probabilities for different trajectories with the same final momentum (−0.8981, 1.232) a.u. as shown by the closed triangle in Fig. 3, and the ionization probabilities near the values 0.39, 0.31, and 0.12 are separately corresponding to the initial conditions (1.0, 0.07, 0.01), (8.82, 0.01, 0.11) and (14.9, 0.17, 0.23) a.u., the closed circle labeled by s_1 and hollow square labeled by s_2 represent the equivalent phases and probabilities for trajectories with the larger and smaller ionization probabilities, respectively. [(b)–(d)] Typical trajectories for ionization time $t_i = 1.0$, 8.82, and 14.9 a.u., respectively. The black arrows indicate the movement direction of the ionized electron.

Figures 4(b) and 4(c) show the typical trajectories for ionization time $t_i = 9.96$ a.u. and 15.4 a.u., respectively. One can see that the two trajectories are very similar: the electron starts from the tunnel exit, but ends up with a parallel momentum in the same direction, and the transverse momentum p_x changes sign by undergoing soft collisions, such as those seen in [55]. They are known as the forward-scattered trajectories [48,55]. At same time, there exists an obvious difference at the origin for the two typical trajectories. In Fig. 4(b), electrons with the near-zero initial transverse momenta are scattered with the large angle by the ionic potential in the direction of the laser polarization as predicted in [44], and this trajectory plays an crucial role in the ionization process. While the electrons with large initial transverse momenta are first decelerated by the laser field with opposite direction, and then are deflected by passing the core, as shown in Fig. 4(c). The above typical trajectories are similar to that of the inner spiderlike structure [29,36], and are obviously different with that of the typical holographic structures such as fishbonelike pattern [27]. Similarly, Fig. 5(a) shows the distributions of phases and the corresponding ionization probabilities for trajectories for the final momentum (−0.8981, 1.232) a.u. The equivalent trajectory s_1 is from the contributions of electron ionized at both $t_i = 1.0$ a.u. and 8.82 a.u., as marked by the closed circle in Fig. 5(a), and the other equivalent trajectory s_2 is from the contributions of electrons ionized born at $t_i = 14.90$ a.u., as marked by the hollow square. It is shown that the ionization probabilities of the two equivalent trajectories s_1 and s_2 are 0.69 and 0.39, respectively, and their phase difference is approximately equal to π, which results in the destructive interference. There exist three typical trajectories, as shown in Figs. 5(b)–5(d). In Fig. 5(b), the electrons with the near-zero initial momenta are first driven in the polarization direction, and then the longitudinal momentum is changed twice, subsequently the electrons are accelerated and undergo hard collisions with the core. Also, the trajectories shown in Figs. 5(c) and 5(d) are much similar to that in Figs. 4(b) and 4(c), respectively. The three typical trajectories possess final phase difference equal to π as shown in Fig. 5(a), and these electrons can arrive at the detector with the same momentum, which cause the destructive interference. We have noted that these trajectories are very close to the core during the collision, so scattered electrons carry the information about the core. Hence this structure caused by the large angle scattering can be also used to image the structure of the target as reported in [17,25,27]. Further, according to the above analysis in Figs. 4 and 5, it is concluded that the gross structure of the oblique interference arises from the forward-scattered electron ionized within a quarter-cycle of the fundamental field. This structure is distinctly different from the holographic interference structure induced by the interference between the direct and scattered trajectories [15,37]. Next the fine interference structure will be discussed. The momenta $(-0.8531, 1.348)$ a.u. and $(-0.8456, 1.348)$ a.u. on the adjacent constructive and destructive fine stripes in Fig. 3(b) are used as samples. Figures 6(a) and 6(b) show distributions of phases and the corresponding ionization probabilities for the final momentum (a) $(-0.8531, 1.348)$ a.u. and (b) $(-0.8456, 1.348)$ a.u. Figure 6(a) shows that the ionization probabilities of the equivalent trajectories s_1 and s_2 are comparable, and their phase difference is smaller than $\pi/2$, which lead to the constructive interference. Here we have neglected the trajectories with lower ionization smaller than 0.1. In Fig. 6(b), because the phase difference of s_1 and s_2 is about equal to π, the interference is destructive. The above result indicates that electrons born in two adjacent cycles, possessing different phases and approximately equal probabilities but the same final momentum, can give rise to coherent superposition and form the fine interference structure.

B. Dependence of the interference structure on the relative phase

By the above analysis of the scattered electrons' trajectories, it has been demonstrated that the final interference is directly related with the ionization probabilities and accumulated phases of scattered electrons. The gross structure of the oblique structure is attributed to contributions from forward-scattered electrons emitted within a same quarter-cycle of the fundamental field. Further, the probabilities and tunneling times of the ionized electrons are obviously dependent on the synthetic laser field, and can be effectively controlled by the relative phase of two laser fields [56,57]. As a result, the dynamics of the different ionized electrons can be manipulated by the relative phase to produce the certain interference pattern.

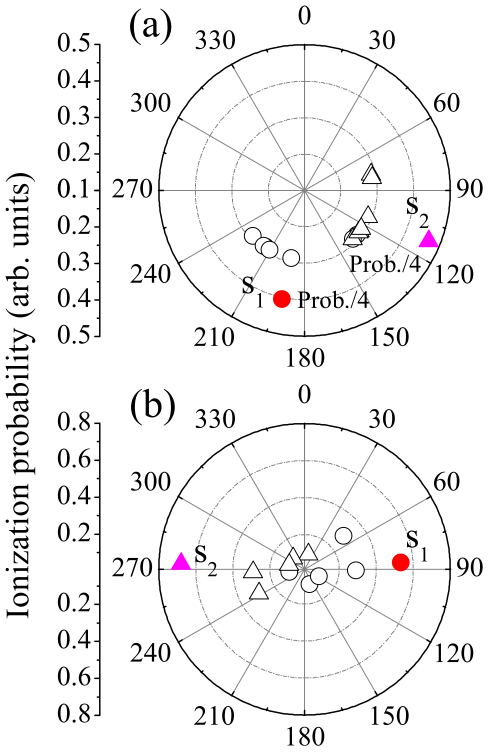

FIG. 6. Distributions of phases and the corresponding ionization probabilities for the final momentum (a) $(-0.8531, 1.348)$ and (b) $(-0.8456, 1.348)$ a.u. The hollow circles and triangles stand for the phases and probabilities of trajectories from scattered electrons A and B, respectively. The closed circle (s_1) and triangle (s_2) represent the equivalent phases and corresponding probabilities from these hollow circles and triangles, respectively.

Despite the intensity of the third-harmonic laser is low in this paper, the synthetic laser field can be effectively modulated by controlling the relative phase φ, as shown by blue curves in Figs. 7(a) and 7(d) for $\varphi = -0.5\pi$ and 0.5π, respectively. One can see that the peaks positions of the laser field are obviously shifted with different relative phases. Further the PMDs are depicted for $\varphi = -0.5\pi$ [Figs. 7(b) and 7(c)] and $\varphi = 0.5\pi$ [Figs. 7(e) and 7(f)], where Figs. 7(b) and 7(e) are simulated by the TDSE, Figs. 7(c) and 7(f) are simulated by the CCSFA. The results of the TDSE are in good agreement with the corresponding results of the CCSFA. It is found that the multiple interference structures in PMDs are sensitively manipulated by the relative phases of two color. The spiderlike interference is more prominent for $\varphi = -0.5\pi$ in Figs. 7(b) and 7(c), while is obscured for $\varphi = 0.5\pi$ in Figs. 7(e) and 7(f). Meanwhile, the fishbonelike interference pattern is enhanced in in Figs. 7(e) and 7(f). It is noted that the oblique interference structure also depends significantly on the relative phase of two colors, where the oblique structure for $\varphi = -0.5\pi$ is enhanced and the structure for $\varphi = 0.5\pi$ is suppressed.

So as to understand the reason that the multiple interference structures are controlled by laser parameters, the initial conditions for the final velocity range 0.8 a.u.$< p_z <$ 2.0 a.u.

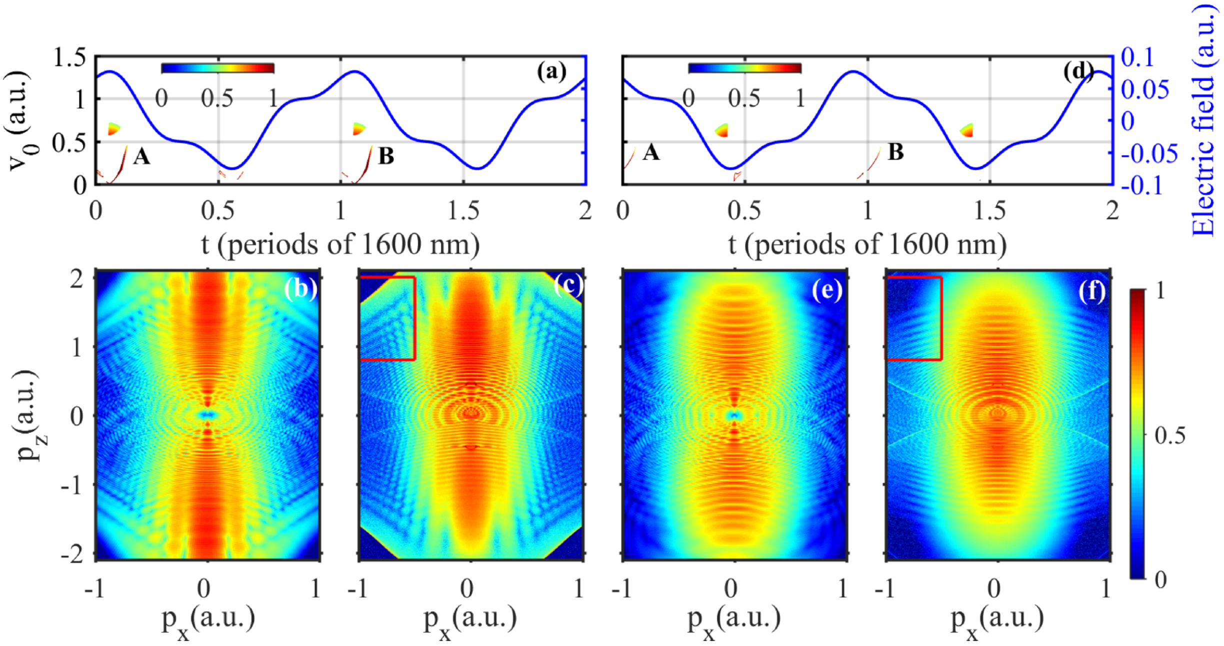

FIG. 7. (a) and (d) show the initial conditions for the final velocity range 0.8 a.u.$< p_z <$ 2.0 a.u. and -1.0 a.u.$< p_x < -0.5$ a.u. as shown by the rectangular areas in (c) and (f), the symbols A and B represent the scattered electrons, and blue curve represents the laser field. [(b), (c)] and [(e), (f)] show PMDs with different relative phases, where (b) and (e) are simulated by the TDSE, and (c) and (f) are simulated by the CCSFA. [(a)–(c)] and [(d)–(f)] are corresponding to relative phases $\varphi = -0.5\pi$ and 0.5π, respectively (on a logarithmic scale).

and -1.0 a.u.$< p_x < -0.5$ a.u. [the rectangular areas in Figs. 7(c) and 7(f)] are shown by the color areas in Figs. 7(a) and 7(d) for $\varphi = -0.5\pi$ and 0.5π, respectively. It is found that the relative ionization times for direct and scattered electrons are controlled by the relative phase, where the ionizations for direct and scattered electrons happen within a same quarter-cycle of the fundamental field for $\varphi = -0.5\pi$. Also, the probabilities of forward-scattered electrons are obviously enhanced when $\varphi = -0.5\pi$. Hence these results may be in favor to the enhancement of the oblique and spider-like interferences for $\varphi = -0.5\pi$. On the other hand, for $\varphi = 0.5\pi$, the fishbonelike structure is enhanced due to the increase of probability for backscattered electrons [15]. By the analogy, the dynamics of other interference patterns can be also manipulated by the relative phase to control the ionized times and the coherent phases of EWPs. Hence it indicates that the two-color laser fields can be tailored with the purpose of manipulating specific dynamics process of ionized electron, which will be helpful to study certain patterns in the multiple interference structure.

Additionally, the fine structure is attributed to the intercycle interference of the forward-scattered trajectories released within the adjacent periods of the fundamental field, the momentum distribution based on Eq. (11) can be simplified by [58]

$$M(\mathbf{p}) \sim \left| \sum_{j=t_{\mathrm{A}},t_{\mathrm{A}}+T_{1600\,\mathrm{nm}}} e^{iS_j} \right|^2 = |e^{iS_1} + e^{iS_2}|^2$$
$$= 2|1 + \cos(\Delta S_{12})|, \tag{12}$$

where t_{A} and $t_{\mathrm{A}} + T_{1600\,\mathrm{nm}}$ stand for the times of electron ionized from A and B respectively, S_j is corresponding action calculated by Eq. (10) for the equivalent trajectory born at $j = t_{\mathrm{A}}$ or $t_{\mathrm{A}} + T_{1600\,\mathrm{nm}}$. ΔS_{12} represents the phase difference between two intercycle trajectories and can be approximated as

$$\begin{aligned}\Delta S_{12} &= \int_{t_1}^{t_1+T_{1600\,\mathrm{nm}}} \left[\frac{1}{2}(\mathbf{p} + \mathbf{A}(\tau))^2 - \frac{Z}{|\mathbf{r}(\tau)|} + I_p\right] d\tau\\ &= (E_k + U_{p1} + U_{p2} + I_p)T_{1600\,\mathrm{nm}}\\ &\quad + \frac{E_1^2 T_{1600\,\mathrm{nm}}}{18\omega^2}\sin^2\varphi + \frac{p_z E_1 T_{1600\,\mathrm{nm}}}{3\omega}\sin\varphi\\ &\quad - \int_{t_1}^{t_1+T_{1600\,\mathrm{nm}}} \frac{Z}{|\mathbf{r}(\tau)|} d\tau.\end{aligned} \tag{13}$$

In the above, $E_k = \mathbf{p}^2/2$ is kinetic energy of the ionized electron, U_{p1} (U_{p2}) is ponderomotive energy of ionized electron from the fundamental (third harmonic) laser field. Equation (13) indicates that the fine structure is dependent on the energy of the ionized electron and Coulomb potential for a certain laser condition. The fringe separation in fine structure decreases with the increase of energy of the ionized electron, as shown in Fig. 3(b).

IV. CONCLUSION

In conclusion, we have studied the multiple interferences in the PMDs and revealed dynamics of these complex structures by solving the TDSE and using CCSFA methods, when xenon atom was exposed to a two-color linearly polarized laser field. The CCSFA simulations reproduce well the main interference features of the TDSE results. Especially, the oblique interference structure was analyzed. By extracting the initial conditions of the ionized electrons, it has been found that the oblique structure is only attributed to the interference from the forward-scattered electrons carrying different phases. Further, the gross interference structure comes from the scattered electron ionized within a quarter-cycle of the fundamental field; the fine structure stems from the intercycle interferences from the forward-scattered electrons. Also, by analyzing the trajectories of the scattered electrons released at different times, it has been demonstrated that the electrons ionized within a quarter-cycle of the fundamental field can be divided into two classes: If the ionization probabilities of the two equivalent trajectories are comparable, and phase difference is approximated to π, they will lead to the destructive interference; if one of the equivalent trajectories makes a dominant contribution to the ionization process, it will result in the appearance of gross interference structure. Moreover, it has been proved that the dynamics of multiple interference structure can be manipulated by relative phase of two colors to produce a certain structure. This structure will boost future research to extract ultrafast-resolved spatio-temporal information from strong-field patterns.

ACKNOWLEDGMENTS

The work was supported by the National Key Research and Development Program of China (Grant No. 2019YFA0307700), the National Natural Science Foundation of China (Grant Nos. 12104285, 91950101, and 12074240), Sino-German Mobility Programme (Grant No. M-0031), and the Open Fund of the State Key Laboratory of High Field Laser Physics (SIOM).

[1] F. Krausz and M. Ivanov, Attosecond physics, Rev. Mod. Phys. **81**, 163 (2009).

[2] P. B. Corkum and F. Krausz, Attosecond science, Nat. Phys. **3**, 381 (2007).

[3] X. Song, S. Gong, W. Yang, S. Jin, X. Feng, and Z. Xu, Coherent control of spectra effects with chirped femtosecond laser pulse, Opt. Commun. **236**, 151 (2004).

[4] W. Yang, X. Song, S. Gong, Y. Cheng, and Z. Xu, Carrier-Envelope Phase Dependence of Few-Cycle Ultrashort Laser Pulse Propagation in a Polar Molecule Medium, Phys. Rev. Lett. **99**, 133602 (2007).

[5] W. Yang, J. Li, W. Jia, H. Zhang, X. Liu, M. Zhu, X. Song, and J. Chen, Effect of the Stark shift on the low-energy interference structure in strong-field ionization, Phys. Rev. A **103**, 053105 (2021).

[6] W. Yang, H. Zhang, C. Lin, J. Xu, Z. Sheng, X. Song, S. Hu, and J. Chen, Momentum mapping of continuum-electron wavepacket interference, Phys. Rev. A **94**, 043419 (2016).

[7] F. Jin, H. Yang, H. Zhang, B. Wang, and W. Yang, Influence of polarization directions of the IR+XUV two-color laser fields on angle-resolved photoelectron energy spectrum, Opt. Express **29**, 10726 (2021).

[8] F. Jin, Y. Tian, J. Chen, Y. Yang, X. Liu, Z.-C. Yan, and B. Wang, Nonsequential double ionization of helium in IR+XUV two-color laser fields: Collision-ionization process, Phys. Rev. A **93**, 043417 (2016).

[9] M.-H. Yuan and X.-B. Bian, Angular distribution of photoelectron momentum in above-threshold ionization by circularly polarized laser pulses, Phys. Rev. A **101**, 013412 (2020).

[10] P. Stammer, S. Patchkovskii, and F. Morales, Evidence of ac-Stark-shifted resonances in intense two-color circularly polarized laser fields, Phys. Rev. A **101**, 033405 (2020).

[11] X. Song, J. Xu, C. Lin, Z. Sheng, P. Liu, X. Yu, H. Zhang, W. Yang, S. Hu, J. Chen *et al.*, Attosecond interference induced by Coulomb-field-driven transverse backward-scattering electron wave packets, Phys. Rev. A **95**, 033426 (2017).

[12] X. Song, R. Zuo, S. Yang, P. Li, T. Meier, and W. Yang, Attosecond temporal confinement of interband excitation by intraband motion, Opt. Express **27**, 2225 (2019).

[13] Y. Huismans, A. Rouzée, A. Gijsbertsen, J. H. Jungmann, A. S. Smolkowska, P. S. W. M. Logman, F. Lépine, C. Cauchy, S. Zamith, T. Marchenko *et al.* Time-resolved holography with photoelectrons, Science **331**, 61 (2011).

[14] Y. Huismans, A. Gijsbertsen, A. S. Smolkowska, J. H. Jungmann, A. Rouzée, P. S. W. M. Logman, F. Lépine, C. Cauchy, S. Zamith, T. Marchenko, J. M. Bakker, G. Berden, B. Redlich, A. F. G. van der Meer, M. Yu. Ivanov, T.-M. Yan, D. Bauer, O. Smirnova, and M. J. J. Vrakking, Scaling Laws for Photoelectron Holography in the Midinfrared Wavelength Regime, Phys. Rev. Lett. **109**, 013002 (2012).

[15] X. B. Bian, Y. Huismans, O. Smirnova, K. J. Yuan, M. J. J. Vrakking, and A. D. Bandrauk, Subcycle interference dynamics of time-resolved photoelectron holography with midinfrared laser pulses, Phys. Rev. A **84**, 043420 (2011).

[16] C. Figueira de Morisson Faria and A. S. Maxwell, It is all about phases: Ultrafast holographic photoelectron imaging, Rep. Prog. Phys. **83**, 034401 (2020).

[17] M. M. Liu, M. Li, C. Wu, Q. Gong, A. Staudte, and Y. Liu, Phase Structure of Strong-Field Tunneling Wave Packets from Molecules, Phys. Rev. Lett. **116**, 163004 (2016).

[18] J. Tan, Y. Zhou, M. He, Y. Chen, Q. Ke, J. Liang, X. Zhu, M. Li, and P. Lu, Determination of the Ionization Time Using Attosecond Photoelectron Interferometry, Phys. Rev. Lett **121**, 253203 (2018).

[19] S. Eckart, Holographic angular streaking of electrons and the Wigner time delay, Phys. Rev. Research **2**, 033248 (2020).

[20] M. He, Y. Li, Y. Zhou, M. Li, W. Cao, and P. Lu, Direct Visualization of Valence Electron Motion Using Strong-Field Photoelectron Holography, Phys. Rev. Lett. **120**, 133204 (2018).

[21] S. Walt, N. Ram, M. Atala, N. Shvetsov-Shilovski, A. von Conta, D. Baykusheva, M. Lein, and H. Wörner, Dynamics of valence-shell electrons and nuclei probed by strong-field holography and rescattering, Nat. Commun. **8**, 15651 (2017).

[22] X. Xie, Two-Dimensional Attosecond Electron Wave-Packet Interferometry, Phys. Rev. Lett. **114**, 173003 (2015).

[23] X. Song, C. Lin, Z. Sheng, P. Liu, Z. Chen, W. Yang, S. Hu, C. D. Lin, and J. Chen, Unraveling nonadiabatic ionization and Coulomb potential effect in strong-field photoelectron holography, Sci. Rep. **6**, 28392 (2016).

[24] Y. Zhou, O. I. Tolstikhin, and T. Morishita, Near-Forward Rescattering Photoelectron Holography in Strong-Field Ionization: Extraction of the Phase of the Scattering Amplitude, Phys. Rev. Lett. **116**, 173001 (2016).

[25] H. Kang, A. S. Maxwell, D. Trabert, X. Lai, S. Eckart, M. Kunitski, M. Schöffler, T. Jahnke, X. Bian, R. Dörner, and C. Figueira de Morisson Faria, Holographic detection of parity in atomic and molecular orbitals, Phys. Rev. A **102**, 013109 (2020).

[26] W. Yang, Z. Sheng, X. Feng, M. Wu, Z. Chen, and X. Song, Molecular photoelectron holography with circularly polarized laser pulses, Opt. Express **22**, 2519 (2014).

[27] X. B. Bian and A. D. Bandrauk, Attosecond Time-Resolved Imaging of Molecular Structure by Photoelectron Holography, Phys. Rev. Lett. **108**, 263003 (2012).

[28] M. Möller, F. Meyer, A. M. Sayler, G. G. Paulus, M. F. Kling, B. E. Schmidt, W. Becker, and D. B. Milošević, Off-axis low-energy structures in above-threshold ionization, Phys. Rev. A **90**, 023412 (2014).

[29] D. D. Hickstein, P. Ranitovic, S. Witte, X.-M. Tong, Y. Huismans, P. Arpin, X. Zhou, K. E. Keister, C. W. Hogle, B. Zhang, C. Ding, P. Johnsson, N. Toshima, M. J. J. Vrakking, M. M. Murnane, and H. C. Kapteyn, Direct Visualization of Laser-Driven Electron Multiple Scattering and Tunneling Distance in Strong-Field Ionization, Phys. Rev. Lett. **109**, 073004 (2012).

[30] C. I. Blaga, F. Catoire, P. Colosimo, G. G. Paulus, H. G. Muller, P. Agostini, and L. F. DiMauro, Strong-field photoionization revisited, Nat. Phys. **5**, 335 (2009).

[31] Ph. A. Korneev, S. V. Popruzhenko, S. P. Goreslavski, T.-M. Yan, D. Bauer, W. Becker, M. Kübel, M. F. Kling, C. Rödel, M. Wünsche, and G. G. Paulus, Interference Carpets in Above-Threshold Ionization: From the Coulomb-Free to the Coulomb-Dominated Regime, Phys. Rev. Lett. **108**, 223601 (2012).

[32] C. M. Maharjan, A. S. Alnaser, I. Litvinyuk, P. Ranitovic, and C. L. Cocke, Wavelength dependence of momentum-space images of low-energy electrons generated by short intense laser pulses at high intensities, J. Phys. B: At. Mol. Opt. Phys. **39**, 1955 (2006).

[33] T. Marchenko, H. G. Muller, K. J. Schafer, and M. J. J. Varkking, Wavelength dependence of photoelectron spectra in above-threshold ionization, J. Phys. B: At. Mol. Opt. Phys. **43**, 185001 (2010).

[34] M. Haertelt, X. B. Bian, M. Spanner, A. Staudte, and P. B. Corkum, Probing Molecular Dynamics by Laser-Induced Backscattering Holography, Phys. Rev. Lett. **116**, 133001 (2016).

[35] M. Li, X. Sun, X. Xie, Y. Shao, Y. Deng, C. Wu, Q. Gong, and Y. Liu, Revealing backward rescattering photoelectron interference of molecules in strong infrared laser fields, Sci. Rep. **5**, 8519 (2015).

[36] A. S. Maxwell, A. Al-Jawahiry, T. Das, and C. Figueira de Morisson Faria, Coulomb-corrected quantum interference in above-threshold ionization: Working towards multitrajectory electron holography, Phys. Rev. A **96**, 023420 (2017).

[37] X. Lai, S. Yu, Y. Huang, L. Hua, C. Gong, W. Quan, C. Figueira de Morisson Faria, and X. Liu, Near-threshold photoelectron holography beyond the strong-field approximation, Phys. Rev. A **96**, 013414 (2017).

[38] S. Eckart, M. Kunitski, I. Ivanov, M. Richter, K. Fehre, A. Hartung, J. Rist, K. Henrichs, D. Trabert, N. Schlott, L. Ph. H. Schmidt, T. Jahnke, M. S. Schöffler, A. Kheifets, and R. Dörner, Subcycle interference upon tunnel ionization by counter-rotating two-color fields, Phys. Rev. A **97**, 041402(R) (2018).

[39] V.-H. Hoang, V.-H. Le, C. D. Lin, and A.-T. Le, Retrieval of target structure information from laser-induced photoelectrons by few-cycle bicircular laser fields, Phys. Rev. A **95**, 031402(R) (2017).

[40] M. Richter, M. Kunitski, M. Schöffler, T. Jahnke, L. P. H. Schmidt, M. Li, Y. Liu, and R. Dörner, Streaking Temporal Double-Slit Interference by an Orthogonal Two-Color Laser Field, Phys. Rev. Lett. **114**, 143001 (2015).

[41] Y. Huang, J. Zhao, Z. Shu, Y. Zhu, J. Liu, W. Dong, X. Wang, Z. Lü, D. Zhang, J. Yuan, J. Chen, and Z. Zhao, Ultrafast hole deformation revealed by molecular attosecond interferometry, Ultrafast Sci. **2021**, 9837107 (2021).

[42] X. Gong, C. Lin, F. He, Q. Song, K. Lin, Q. Y. Ji, W. Zhang, J. Ma, P. Lu, Y. Liu, H. Zeng, W. Yang, and J. Wu, Energy-Resolved Ultrashort Delays of Photoelectron Emission Clocked by Orthogonal Two-Color Laser Fields, Phys. Rev. Lett. **118**, 143203 (2017).

[43] X. Song, G. Shi, G. Zhang, J. Xu, C. Lin, J. Chen, and W. Yang, Attosecond Time Delay of Retrapped Resonant Ionization, Phys. Rev. Lett. **121**, 103201 (2018).

[44] X. Liu, G. Zhang, J. Li, G. Shi, M. Zhou, B. Huang, Y. Tang, X. Song, and W. Yang, Deep Learning for Feynman's Path Integral in Strong-Field Time-Dependent Dynamics, Phys. Rev. Lett. **124**, 113202 (2020).

[45] V. Mosert and D. Bauer, Photoelectron spectra with Qprop and t-SURFF, Comput. Phys. Commun. **207**, 452 (2016).

[46] W. Gordon, Der Comptoneffekt nach der Schrödingerschen Theorie, Z. Phys. **40**, 117 (1926).

[47] D. M. Wolkow, Über eine Klasse von Lösungen der Diracschen Gleichung, Z. Phys. **94**, 250 (1935).

[48] T. M. Yan, S. V. Popruzhenko, M. J. J. Vrakking, and D. Bauer, Low-Energy Structures in Strong Field Ionization Revealed by Quantum Orbits, Phys. Rev. Lett. **105**, 253002 (2010).

[49] T. M. Yan and D. Bauer, Sub-barrier Coulomb effects on the interference pattern in tunneling-ionization photoelectron spectra, Phys. Rev. A **86**, 053403 (2012).

[50] D. B. Milošević, G. G. Paulus, D. Bauer, and W. Becker, Above-threshold ionization by few-cycle pulses, J. Phys. B: At. Mol. Opt. Phys. **39**, R203(R) (2006).

[51] V. S. Popov, Imaginary-time method in quantum mechanics and field theory, Phys. At. Nucl. **68**, 686 (2005).

[52] D. G. Arbó, S. Yoshida, E. Persson, K. I. Dimitriou, and J. Burgdörfer, Interference Oscillations in the Angular Distribution of Laser-Ionized Electrons near Ionization Threshold, Phys. Rev. Lett. **96**, 143003 (2006).

[53] P. Agostini, F. Fabre, G. Mainfray, G. Petite, and N. K. Rahman, Free-Free Transitions Following Six-Photon Ionization of Xenon Atoms, Phys. Rev. Lett. **42**, 1127 (1979).

[54] Here we only consider the trajectories with the ionization probability more than 0.01, the other trajectories are neglected due to much smaller probability.

[55] A. S. Maxwell and C. Figueira de Morisson Faria, Coulomb-free and Coulomb-distorted recolliding quantum orbits in photoelectron holography, J. Phys. B: At. Mol. Opt. Phys. **51**, 124001 (2018).

[56] S. Skruszewicz, J. Tiggesbäumker, K.-H. Meiwes-Broer, M. Arbeiter, Th. Fennel, and D. Bauer, Two-Color Strong-Field Photoelectron Spectroscopy and the Phase of the Phase, Phys. Rev. Lett. **115**, 043001 (2015).

[57] S. Luo, M. Li, H. Xie, P. Zhang, S. Xu, Y. Li, Y. Zhou, P. Lan, and P. Lu, Angular-dependent asymmetries of above-threshold ionization in a two-color laser field, Phys. Rev. A **96**, 023417 (2017).

[58] Y. Feng, M. Li, S. Luo, K. Liu, B. Du, Y. Zhou, and P. Lu, Semiclassical analysis of photoelectron interference in a synthesized two-color laser pulse, Phys. Rev. A **100**, 063411 (2019).